

Soil Compensation Techniques for the Detection of Buried Metallic Objects Using Electromagnetic Sensors

Leonard R. Pasion^{ab}, Douglas W. Oldenburg^a, Stephen D. Billings^b, and David Sinex^a

^aUniv. of British Columbia Geophysical Inversion Facility,
6339 Stores Road, Vancouver, BC, V6T-1Z4, CANADA;

^bSky Research Inc., 112A/2386 East Mall, Vancouver, BC, V6T-1Z3, CANADA

ABSTRACT

Magnetic soils are a major source of false positives when searching for landmines or unexploded ordnance (UXO) with electromagnetic induction sensors. In adverse areas up to 30% of identified electromagnetic (EM) anomalies are attributed to geology. The main source of the electromagnetic response is the magnetic viscosity of the ferrimagnetic minerals magnetite and maghaemite. The EM phenomena that give rise to the response of magnetically viscous soil and metal are fundamentally different. The viscosity effects of magnetic soil can be accurately modelled by assuming a ferrite relaxation with a log-uniform distribution of time constants. The EM response of a metallic target is due to eddy currents induced in the target and is a function of the target's size, shape, conductivity and magnetic susceptibility. In this presentation, we consider different soil compensation techniques for time domain and frequency domain EM data. For both types of data we exploit the EM characteristics of viscous remnant magnetized soil. These techniques will be demonstrated with time domain and frequency domain data collected on Kaho'olawe Island, Hawaii. A frequency domain technique based on modeling a negative log-linear in-phase and constant quadrature component was found to be very effective at suppressing false-alarms due to magnetic soils.

Keywords: unexploded ordnance, magnetic soils

1. INTRODUCTION

Remediation of UXO contaminated sites is a multi-stage process consisting of detection, discrimination, and excavation. Detection and identification of UXO using metal detectors can be very difficult at sites with large geologic background signals.¹ These signals are due to sensitivity of electromagnetic sensors to the presence of soils exhibiting viscous remnant magnetization (VRM).²⁻⁴ At sites where soils have a large VRM component, metal detectors measure background responses of the same order of magnitude of UXO. Micro-topographic features such as holes and sensor movement will produce anomalies that have the same spatial wavelength as UXO.⁵

UXO discrimination is achieved by extracting parameters from geophysical data that reflect characteristics of the target that generated the measured signal. The most common approach to applying discrimination to data collected in geologically noisy areas involves: (1) filtering to remove the long wavelength response, and (2) inverting the remaining short spatial wavelength anomalies for parameters of a forward model for a compact metallic target, such as the dipole model. Filtering artifacts will impact the accuracy with which target parameters are recovered. An alternate approach is to invert the unfiltered data with a model that includes the response of the background geology.⁶

This presentation is in two parts. First we attempt to model sensor data using a soil model only. The degree of success, or equivalently the data misfit, helps us determine the soil response and also is an aid target picking. In the second part of the presentation we examine the use of data inversion applied to filtered data for dipole parameters.

Further author information: (Send correspondence to L.R.P.)

L.R.P.: E-mail: len.pasion@skyresearch.com, Telephone: 1 505 123 1234

2. THE MAGNETIC SUSCEPTIBILITY OF A COLLECTION OF VISCOUS REMNANT MAGNETIC PARTICLES

Neel⁷ developed a simple theory to describe the magnetization of an ensemble of non-interacting single domain grains. The time for the magnetization vector of a grain to rotate in the presence of an applied field is quantified by a relaxation time τ . The non-instantaneous acquisition and decay of magnetization requires a complex frequency-dependent susceptibility to explain the behavior of a system exhibiting viscous magnetization. The frequency dependent susceptibility is the one-sided Fourier transform of the impulse response (equivalent to the derivative of the step-off after-affect function).⁸ An elementary Fourier integral can be used to show that for a single relaxation time the complex susceptibility model is

$$\chi(\omega) = \frac{\chi_o}{1 + i\omega\tau} \quad (1)$$

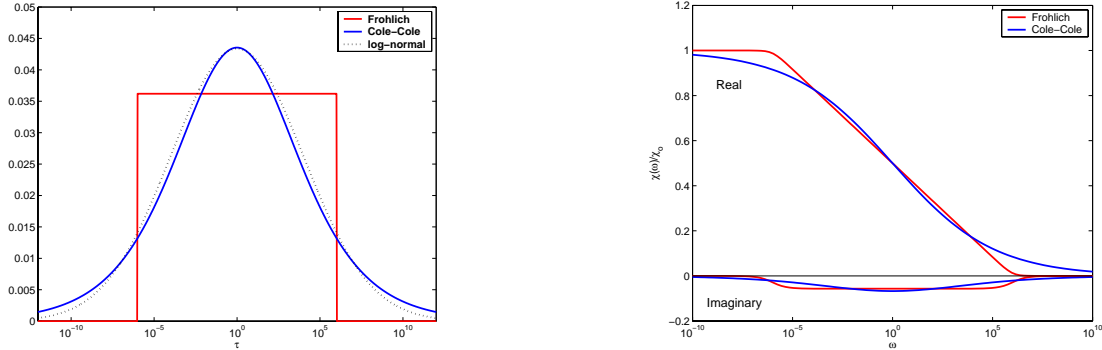
This model is the well known Debye model. In more general terms, if the relaxation times are distributed with the weight function $f(\tau)$ then the complex susceptibility model becomes

$$\chi(\omega) = \chi_o \int_0^\infty \frac{f(\tau)}{1 + i\omega\tau} d\tau \quad (2)$$

A log-uniform, or Frohlich, distribution is a common choice for the distribution of time constants.^{2,8} Through a simple change of variables, we can rewrite the $f(\tau)$ in its logarithmic form $G(\ln \tau)$

$$G(\ln \tau) = \begin{cases} \frac{1}{\ln(\tau_1/\tau_2)} & \tau_1 < \tau < \tau_2, \\ 0 & \text{otherwise.} \end{cases} \quad (3)$$

where τ_1 and τ_2 are the lower and upper limits of the time constants. Figure 1(a) plots the log-uniform, or Frohlich, distribution with bounding time constant values of $\tau_1 = 10^{-6}$ and $\tau_2 = 10^6$. Substitution of equation 3



(a) Comparison of a Log-Uniform (or Frohlich), Cole-Cole and Log-Normal distributions. (b) Comparison of the resulting magnetic susceptibility from the distributions in (a).

Figure 1. Comparison of the Log-Uniform (or Frohlich) distribution and the Cole-Cole distribution.

into equation 2 for the complex susceptibility gives

$$\chi(\omega) = \chi_o \left(1 - \frac{1}{\log(\tau_2/\tau_1)} \log \left(\frac{1 + i\omega\tau_2}{1 + i\omega\tau_1} \right) \right) \quad (4)$$

Within a certain range of frequencies determined by the end-member time constants, the in-phase susceptibility will vary linearly with the logarithm of the frequency while the quadrature susceptibility is constant with frequency. Furthermore, for $\tau_2 \gg \tau_1$ the slope of the in-phase and the value of the quadrature susceptibility are related by

$$\frac{\partial \text{Re}[\chi(\omega)]}{\partial \log \omega} = \frac{2}{\pi} \text{Im}[\chi(\omega)] = -\frac{\chi_o}{\log(\tau_2/\tau_1)} \quad (5)$$

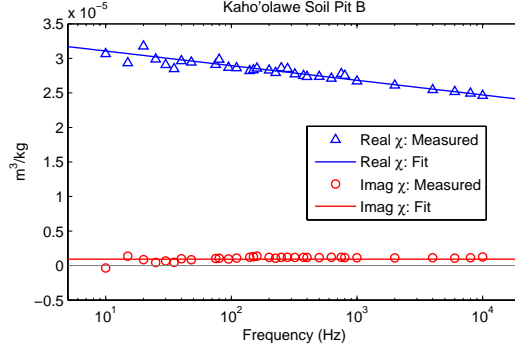


Figure 2. Susceptibility measurement of a soil sample from Kaho'olawe Navy QA grid. The measured susceptibility values are fit assuming a log-uniform time constant susceptibility model.

The Cole-Cole frequency distribution has also been used to represent magnetic susceptibility.^{9,10} The resultant expression is

$$\chi(\omega) = \chi_{\infty} + \frac{\chi_o - \chi_{\infty}}{1 + (i\omega\tau_c)^{1-\alpha}}. \quad (6)$$

where χ_{∞} is the susceptibility as frequency approaches infinity (therefore characterizing the instantaneous magnetization) and χ_o is the susceptibility as frequency approaches zero. The imaginary part of the susceptibility is zero in the limits of zero and infinite frequency. The corresponding expression for the log distribution of the Cole-Cole model is⁸

$$G(\ln \tau) = \frac{1}{2\pi} \frac{\sin(\pi\alpha)}{\cosh((1-\alpha)\ln(\tau_o/\tau)) - \cos(\pi\alpha)} \quad (7)$$

The value of α controls the distribution of relaxation times. The limits of α are $\alpha = 0$ for a single Debye relaxation mechanism and $\alpha = 1$ for an infinitely broad distribution of relaxation times. The time constant τ_c controls the location of the peak of the imaginary part of the susceptibility, with the peak occurring at $\omega = 1/\tau_c$. For a large α the Cole-Cole model yields a straight line for the real part and a constant negative value for the imaginary part, thus it is similar to our model in equation 6. If we assume that $\chi_{\infty} = 0$, $\tau_o = 1$, and $\alpha = 0.83$, we obtain the distribution plotted in blue in Figure 1(a).

It has been suggested that a Log-Normal distribution would best describe the distribution of time constants.¹¹ A log-normal distribution is plotted as a dotted black line in Figure 1. Clearly, the log-normal distribution can be well approximated by a Cole-Cole model with the appropriate parameters. We would expect that the effective magnetic susceptibility would be the same.

The island of Kaho'olawe, Hawaii is well known for the difficulties in detecting buried ordnance due to its heavily weathered, iron-oxide rich soils.¹ Complex susceptibility measurements of a number of soil samples from the Navy UXO QA grid were carried out using a LakeShore Cryotronics AC Susceptometer at the University of Minnesota's Institute for Rock Magnetism (IRM).¹² Figure 2 contains a typical measurement for the Kaho'olawe soil samples. The susceptibility of the Kaho'olawe soil samples exhibit a strongly frequency-dependent real component and a much smaller, and nearly constant, imaginary component. The best fit log-uniform time constant susceptibility model of equation is plotted as a solid line.

3. ELECTROMAGNETIC RESPONSE TO VISCOUS REMNANT MAGNETIC HALFSPACE

Consider a circular transmitter loop of radius a , carrying a current I , and at a height h above a halfspace. At an observation point at the center of the transmitter loop, the secondary field is vertical. For a resistive halfspace, the secondary field is

$$H_z^s(\omega) = \frac{Ia}{2} \left(\frac{\chi}{2 + \chi} \right) \frac{a}{[a^2 + (2h)^2]^{3/2}} \quad (8)$$

In cases where $\chi \ll 1$,

$$H_z^s(\omega) \approx \frac{I}{4} \frac{a^2}{[a^2 + (2h)^2]^{3/2}} \chi(\omega) \quad (9)$$

Therefore the resistive limit response is approximately proportional to the susceptibility. If we represent the magnetic susceptibility with equation 2 and assume that $\tau_2 \gg \tau_1$, then the field can be written as

$$H_z^s(\omega) \approx \frac{I}{4} \frac{a^2}{[a^2 + (2h)^2]^{3/2}} \frac{\chi_o}{\ln(\tau_2/\tau_1)} \left(1 - \ln(\omega\tau_2) - i\frac{\pi}{2}\right) \quad (10)$$

The corresponding result in the time domain can be obtained by taking the sine transform of the imaginary component of the secondary field. The step-off response of the time derivative of the H field is

$$\frac{\partial H}{\partial t} = -\frac{I}{4} \frac{a^2}{[a^2 + (2h)^2]^{3/2}} \frac{\chi_o}{\ln(\tau_2/\tau_1)} \frac{1}{t} \left(e^{-t/\tau_2} - e^{-t/\tau_1}\right) \quad (11)$$

For $t \ll \tau_2$ and $t \gg \tau_1$,

$$\frac{\partial H}{\partial t} \approx -\frac{I}{4} \frac{a^2}{[a^2 + (2h)^2]^{3/2}} \frac{\chi_o}{\ln(\tau_2/\tau_1)} \frac{1}{t} \quad (12)$$

Equations 10 and 12 will be used as soil models.

For constant sensor height and orientation, the measured time domain response and frequency domain response are proportional to $G(\chi) = \chi_o / \log(\tau_2/\tau_1)$. Therefore, in areas of low conductivity soil, electromagnetic sensors act as viscous remnant susceptibility meters. To demonstrate this, we can compare susceptibility measurements with sensor data collected on Kaho'olawe. As part of SERDP project MM-1414,¹² surface soil samples were collected from Grid 2E and their susceptibility measured with a Bartington MS2B susceptibility meter. Comparisons of the susceptibility measurements and sensor data are shown in Figure 3. Figure 3(a) is a grid-

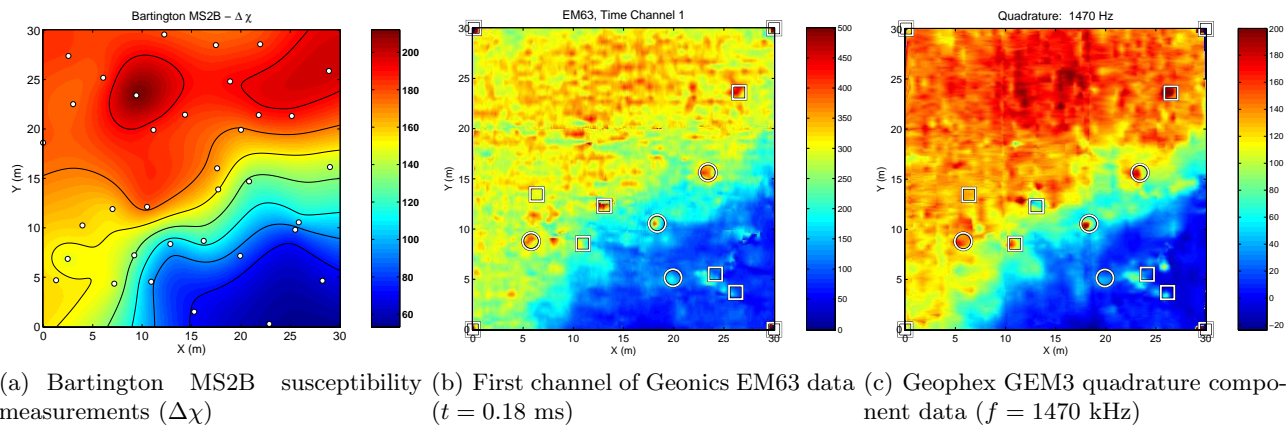


Figure 3. Comparison of Bartington MS2B susceptibility measurements with electromagnetic sensor data. Data collected on the Kaho'olawe Grid 2E are presented.

ded image of the difference in the susceptibility $\Delta\chi$ measured by the Bartington MS2B susceptibility meter at frequencies of 4.7 kHz and 0.47 kHz. If we assume the susceptibility model of equation 2, we can show that the

$$\Delta\chi \approx \frac{\chi_o}{\log(\tau_2/\tau_1)} \log(0.47\text{kHz}/4.7\text{kHz}). \quad (13)$$

EM63 and quadrature component GEM3 data are plotted in Figure 3(b) and (c), respectively. Clearly the three images of Figure 3 are similar to within a scaling factor.

In the frequency domain, the response is proportional to the susceptibility (Equation 9) and not the susceptibility difference. Bartington MS2D measurements were taken on Grid 2E. The Bartington MS2D is a portable susceptibility meter that measures the modulus of the complex susceptibility at frequency $f = 0.98$ kHz. Figure 4 compares measurements from Kaho‘olawe Grid 2E made by the Bartington MS2D sensor with the amplitude of the GEM3 data at 1470 Hz. Both the GEM3 and Bartington measurements identify an increase in signal in the lower right portion of the grid that was not evident in Figure 3. This increase in signal is not seen in the susceptibility and sensor data of Figure 3 since the increase is likely due to an increase in the static susceptibility.

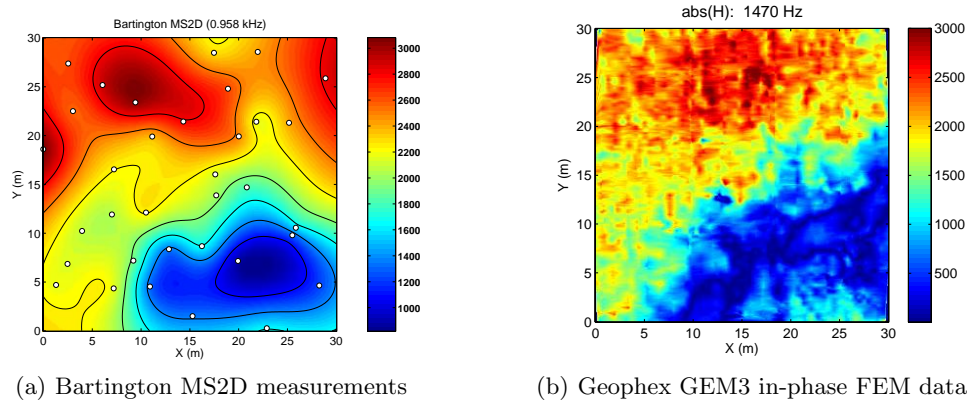


Figure 4. Comparison of Bartington MS2D susceptibility measurements with the inphase component of GEM3 data. The MS2D measures the phasor sum of the complex susceptibility at $f = 0.98$ kHz.

4. TARGET PICKING TECHNIQUES FOR MULTI CHANNEL ELECTROMAGNETIC INDUCTION DATA

The goal of target picking is to generate a list of survey locations at which there is a high probability that a target is present. Target picking is an example of signal detection theory and hypothesis testing. The null hypothesis \mathcal{H}_0 is that the signal is due to noise. In this case, we define the noise to be the random baseline noise of the instrument and the spatially correlated signal from topography and sensor movement. The alternative hypothesis \mathcal{H}_1 is that the signal is from a buried target. Let $p(x|\mathcal{H}_0)$ be the pdf of x under \mathcal{H}_0 , i.e. the pdf of the noise. The variable x is some test statistic of the data. Let $p(x|\mathcal{H}_1)$ be the pdf of x under \mathcal{H}_1 , i.e. the pdf of the target. For a threshold level τ , the probability of false alarm is $P_{FA} = P[x > \tau; \mathcal{H}_0]$ and the probability of detection is $P_D = P[x > \tau; \mathcal{H}_1]$. The definitions of P_D and P_{FA} are expressed graphically in Figure 5. In general, types of targets to be found in a survey are not known ahead of time, so $p(x|\mathcal{H}_1)$ is generally unknown. In this case, the natural approach is to simply sort prospective targets by there probability of false alarm.

In general, target picking involves identifying soundings on a data map whose amplitude exceeds some threshold. Clearly, setting the test statistic to the data amplitude would have only limited success at highly magnetic sites. One approach is to compare the measured data to a soil model. In cases, where a soil model does not fit the data, the sounding is assigned a higher probability of being a UXO, or conversely, a lower probability of false alarm. To demonstrate the effectiveness of this approach we consider a 40 mm M385 projectile buried at a depth of 25 cm. The 40 mm M385 has an aluminum body with a copper rotating band, and is 179 mm in length (Figure 5(a)). Synthetic Geonics EM63 time domain electromagnetic data were created by forward modelling the characteristic polarization tensor for the 40 mm obtained through test stand measurements. The height of the transmitter coil is 30 cm, the depth of the 40 mm is 25 cm, and the orientation is random. We assume that there are two components of the background geologic response: (1) A long wavelength variation due to changes in magnetic susceptibility associated with geologic and/or weathering features, and (2) Short wavelength variations due to topography and sensor motion relative to the surface. For this example we assume that the long wavelength background geology has a mean response of 20 mV. The shorter wavelength background response is simulated by using correlated random numbers.¹³ The smaller wavelength variations in the background response

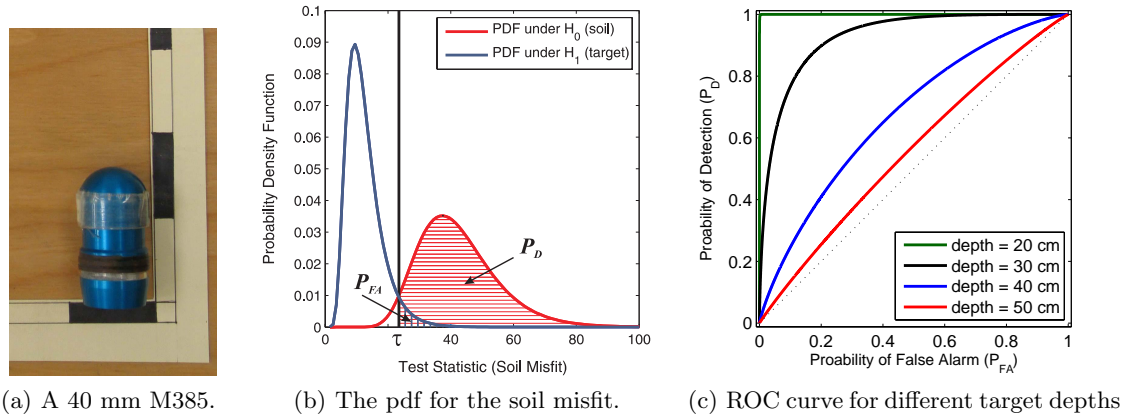


Figure 5. Soil fitting results for data simulated for a 40 mm projectile buried at a depth of 25 cm and in a background geology whose mean response is 20 mV.

are simulated from the power spectra from the Kaho‘olawe test plot data. The standard deviation of the small wavelength background response is set to be 15 percent of the background response. In addition to the soil noise, a background sensor noise with a standard deviation exhibiting a $1/\sqrt{t}$ decay is added to the data. This decay is characteristic of log-gating and stacking white noise.¹⁴ The amplitude of the background is based on measurements from a previous Geonics EM63 survey.¹⁵

A soil model is fit to each of the synthetically generated soundings. For the target fits in this example, we consider soundings directly over the 40 mm target. The fitting procedure involves solving for a soil model that minimizes the least squares misfit between the measured sounding and soil response. The soil response is given by a characteristic soil decay multiplied by an amplitude A , i.e. $\mathcal{F}^{soil} = \mathcal{F}[A] = Af(t)$. Therefore, the fitting involves solving for a single amplitude parameter A . The pdf for the soil and 40 mm projectiles are plotted in Figure 5(b). The soil and 40 mm pdfs are well represented by a log-normal distribution. The ability to accurately pick target depends on the separation and widths of the soil and 40 mm pdfs. As the overlap of the soil and target pdf’s decrease, so does the probability of false negatives and misses.

For a given geologic setting (and therefore soil pdf) the effectiveness of target picking relies on (1) the similarity of the target response to the soil model and (2) the signal strength. The main influence on signal strength is the depth of the target. The ROC curve for a number of different 40 mm depths are plotted in Figure 5(c). The ROC curve is diagnostic of the performance of a classifier as a tradeoff between the probability of false alarm and probability of detection. The ROC curve shows that a 40 mm at 50 cm has a ROC curve that nearly follows the line $P_{FA} = P_D$, which indicates that when the 40 mm is at 50 cm deciding whether a anomaly is due to soil or a target with soil misfit will not perform much better than simply flipping a coin. In contrast, a 40 mm at 20 cm has the perfect rock curve, with no false alarms prior to picking every all the targets.

4.0.1. Fitting TEM data on Kaho‘olawe

Naeva Geophysics, Inc. collected Geonics EM63 data at the ESTCP test site on Kaho‘olawe. Data on Grids 2D and 2E were collected on 60 m long, east-west lines with a linespacing of 50 cm. Data were collected in three 10 m wide sections. Before and after each section, calibration data were collected with the EM63 sensor elevated such that an in air measurement could be recorded, and sensor drift could be estimated and removed.

Figure 6(a) contains gridded images of the soil model misfit ϕ . The different sections of data being joined at $y = 10$ m and $y = 20$ m produce overlapping lines which result in some gridding artifacts. Several of the anomalies in the soil misfit image correspond to buried items. Anomalies not corresponding to emplaced items may be due to a buried metallic target, since it is possible that the site was not completely cleared of metal prior to preparing the test site.

Although it appears that several of the anomalies in Figure 6 correspond to emplaced items, we will not use the image for target picking purposes. Instead, our approach is to determine, for each sounding within the grid,

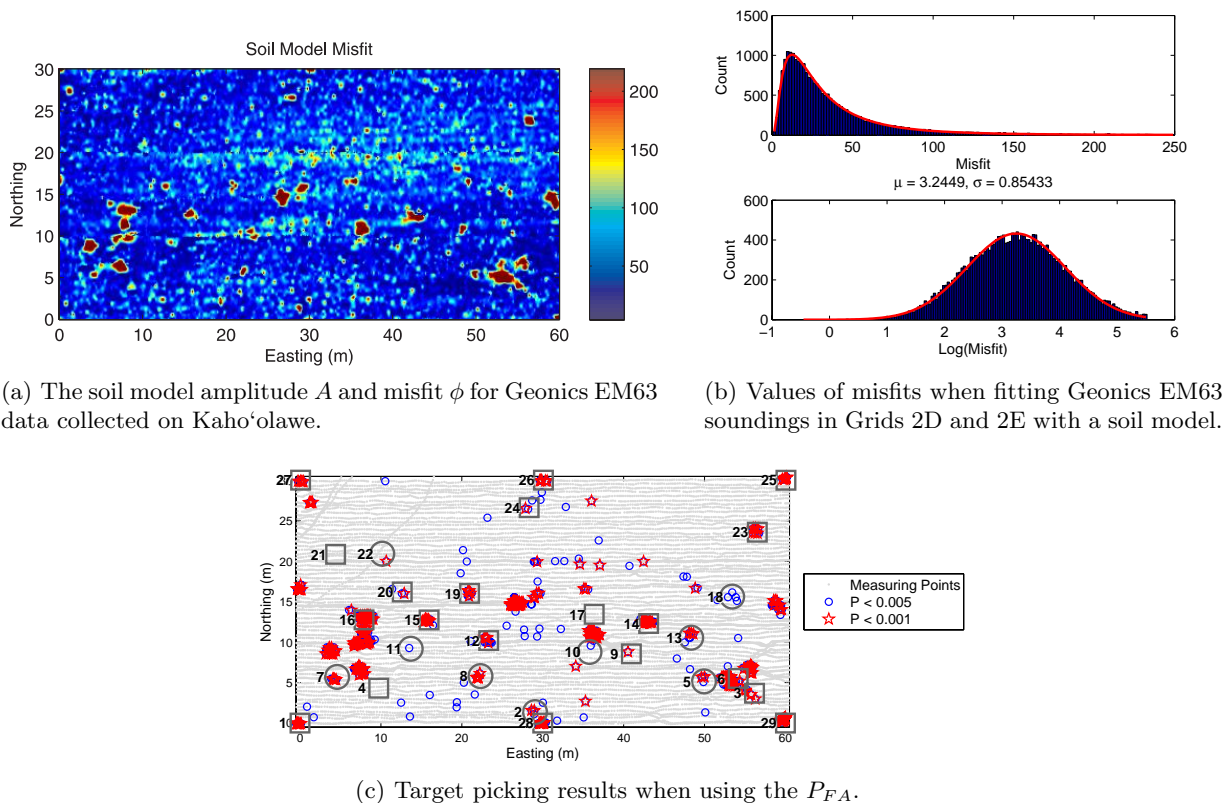


Figure 6. Target picking results using Geonics EM63 time domain electromagnetic data.

the probability that the signal is due to soil (i.e. the null hypothesis). Since we do not have prior knowledge of the target types in the grid, we do not have an estimate of the pdf for the target misfits. Therefore we base our picks on the probability of false alarm P_{FA} . Calculating P_{FA} requires an estimate of the statistics of the soil misfit for the data set. The estimated probability density function and corresponding cumulative distribution function allows us to estimate the probability of false alarm P_{FA} for each sounding. That is, if a sounding has a soil misfit that is unlikely to belong to the distribution of soil misfits, then it will be classified as a target.

Figure 6(b) contains plots of the misfit distributions. The upper plot shows a histogram of the raw misfit values and the lower plot shows a histogram of the log of the misfit values. Values of misfit greater than 250 are considered to be non-soil and are therefore not included when calculating the distribution statistics. Similar to the synthetic data results, the distribution of misfit values are well modelled with a log normal distribution. The mean of $\log(\phi)$ is 3.24 and its standard deviation is 0.85. The red lines plotted on the histograms are distributions with this mean and standard deviation. For each sounding a best fit soil model is calculated, and the misfit of the soil model is used to calculate probability of false alarm P_{FA} .

Figure 6(c) plots results of target picking according to P_{FA} . Grey dots mark locations of each sounding and the emplaced items are indicated by circles (fragments and scrap items) and squares (ordnance items or corner grid stakes). Two thresholds for P_{FA} are plotted; soundings with $P_{FA} < 0.005$ are identified by blue circles, and soundings with $P_{FA} < 0.001$ are identified by red stars. A good target picking algorithm would be able to identify all the known targets (i.e. minimizing false negatives), with a minimal number of picked targets resulting from non-metallic items (i.e. false positives). It is difficult to determine the number of false positives in this example, since there are possibly targets present that were not cleared prior to preparing the test site. In any case, let us compare the picked targets with the locations of the known emplaced items. Setting a threshold of $P_{FA} < 0.005$ results in correctly locating all but 3 items: Targets 4, 17, and 21. Target 21 is a Shoulder launched Multi-purpose Assault Weapon (SMAW) Rocket. A SMAW rocket has a diameter of 84 mm. This particular

rocket was reported to be buried at 76 cm which, due to its size, would be difficult to detect. Target 17 is a 20 mm projectile at a depth of 15 cm. Missing the 20 mm projectile is not unexpected, as the spatial size of the anomaly and the anomaly magnitude would be quite small. Target 4 is listed as a MK-82 at a depth of 1.22 m, which would be at the detection limit for a Geonics EM63 sensor. However, the MK-82 is a type of 500 lb bomb that is 2.21 m long and 10.75 inches (221 mm) in diameter. There are a few reasons why the target picking might not of been able to identify the MK-82. It is possible that the anomaly within a couple of meters to the northwest of the groundtruth location is due to the buried MK-82. In addition, the MK-82 buried may be corroded, and thus have a weak signal.

When using $P_{FA} < 0.005$ as a threshold, we see that there are a number of false positives. Decreasing the threshold to 0.001 (red stars) reduces the number of false positives to 7, but also increases the number of misses. In particular, targets 11 and 18 are no longer picked when the threshold is decreased. For these data, rather than decreasing the threshold to reduce false positives, it would be a better idea to recognize that, for a sufficient spatial coverage, targets generally have more than one sounding in which the soil misfit is large. If we look at the false positives for the $P_{FA} < 0.005$ target list, we see that majority of them are isolated soundings. Removing target picks associated with isolated soundings having a poor misfit reduces the number of false positives, but also results in Targets 9, 11, and 22 no longer being picked as targets.

4.0.2. Fitting FEM data on Kaho'olawe

Frequency domain electromagnetic data were collected at Kaho'olawe using the Geophex GEM-3 sensor. The GEM-3 consists of a co-axial transmitter and receiver loops that simultaneously collects the frequency domain response at frequencies determined by the operator.¹⁶ For the ESTCP demonstration the GEM-3 was mounted on a wheeled cart, and configured to collect data at 10 frequencies located at 90, 150, 390, 750, 1470, 2970, 5910, 11910, 23850 and 47940 Hz. A 1 m circular transmitter loop was used. Data were collected by Geophex Ltd. and they provided us with sensor drift collected data from grid 2E. Grid 2E was surveyed in 3 parts. Each section was 10 m wide, with lines running in a north-south direction with a line spacing of 0.5 m.

We process the GEM3 data by fitting each FEM sounding with the following soil model:

$$\Re(H_z^s(\omega)) = m_1 \ln(\omega) + m_2 \quad \text{and} \quad \Im(H_z^s(\omega)) = m_1 \quad (14)$$

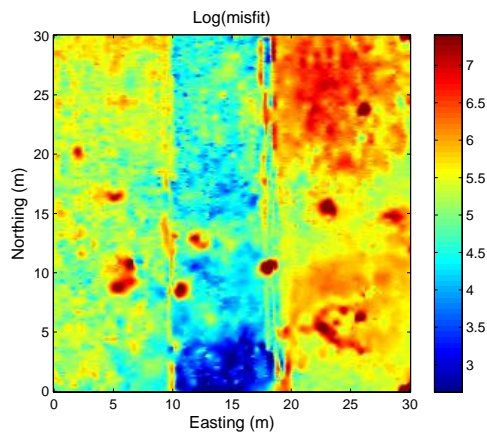
Therefore, we have a two element model vector $\mathbf{m} = [m_1, m_2]^T$ which we estimate through minimizing a least squares objective function. The gridded image of the log of the soil misfit ($\log(\phi)$) is plotted in Figure 7.

Figure 7 clearly shows the three separate surveys that make up the Grid 2E data. The noise characteristics of the instrument are clearly different for each survey. Since the soil misfit distributions for the GEM data are different for each of the three sections, we calculate a soil misfit distribution for each section. Figure 7(b) contain the histograms for the soil misfit in each of the three surveys. The histograms are fit with log normal distributions, and their respective cumulative distributions are computed (Figure 7(c)).

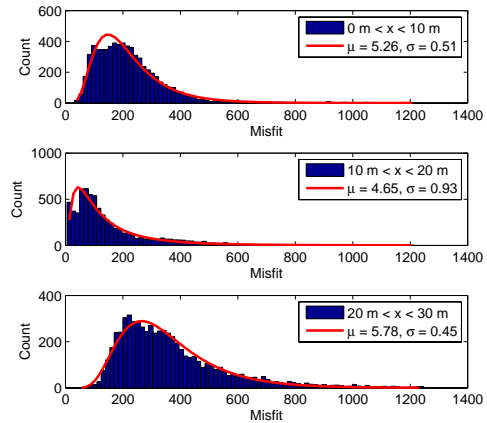
Figure 7(d) shows target picking results with two threshold values: $P_{FA} < 0.001$ and $P_{FA} < 0.005$. The picked targets correspond well with the ground truth. Target 17, a 20 mm projectile buried at a depth of 15 cm, was the only non-scrap emplaced item undetected by this method. Due to its small size, Target 17 was also missed when the target picking technique was applied to the Geonics EM63 data. Target 5 was undetected, but, after taking a closer look at the GEM3 sounding positions in the vicinity of the target, the miss may be due to inadequate spatial coverage. Target 9 (81 mm) is clearly identified by the picking method, although it was missed when processing the EM63 data.

5. ESTIMATION DIPOLE POLARIZATION PARAMETERS FROM FILTERED DATA

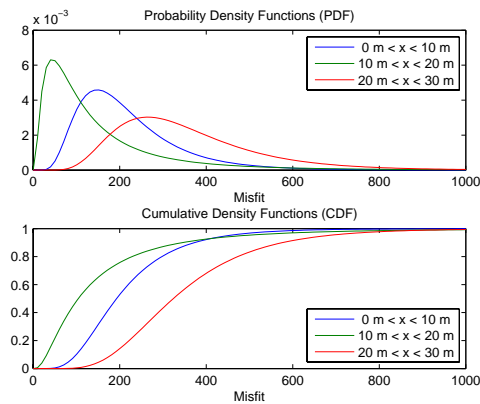
Discrimination is the process of determining, for each anomaly in the target list, the likelihood of being a UXO. The objective is to minimize the number of false negatives and, therefore, unnecessary excavations. UXO discrimination is achieved by extracting parameters from geophysical data that reflect characteristics of the target that generated the measured signal. These parameters come in two forms: (1) data-based parameters that are directly inferred from the data, such as amplitude and energy and (2) model-based parameters that are variables



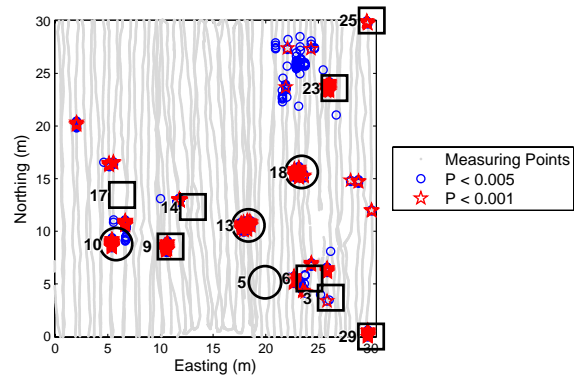
(a) Log of the soil misfit



(b) Histograms for the 3 surveys of Grid 2E.



(c) Probability density functions and cumulative density functions for the soil misfit.

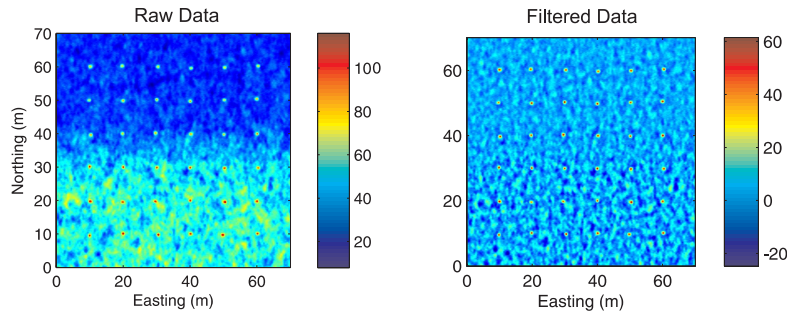


(d) Target picking results when using P_{FA} for detection. The positions of the GEM3 sensor are indicated by grey points.

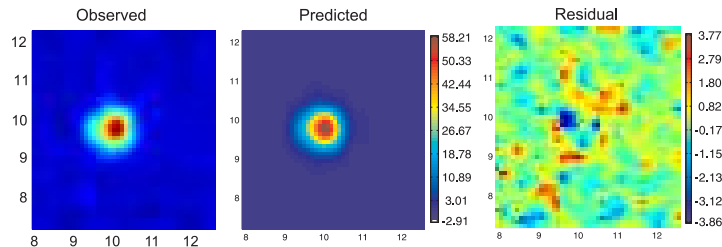
Figure 7. Target picking results using GEM3 data.

of a mathematical forward model that can reproduce the data. Forward models with parameters that are related to the physical properties of an object are referred to as physics-based forward models. Model-based parameters are recovered from inversion of the geophysical data. The dipolar nature of the electromagnetic responses of compact metallic objects measured with sensor/target geometries typical for UXO surveys has lead to a number of techniques for estimating the elements of the magnetic polarization tensor that define the induced dipole strength. These dipole model based techniques have shown great promise for discrimination.^{17–19} The magnetic polarization tensor's components are functions of the size, shape, and material properties of the buried target of interest and therefore provide a model vector from which the target characteristics can be inferred. Target identification is then achieved by using the recovered model parameters as part of feature vectors that are input into statistical classification algorithms.^{20–22}

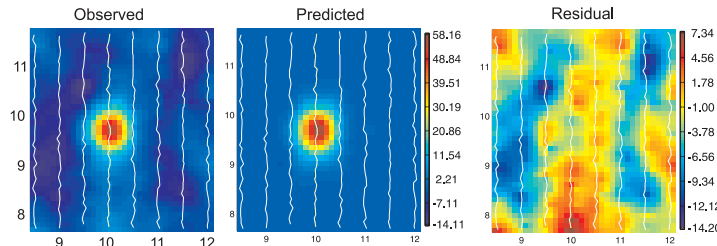
The success of dipole model based discrimination algorithms depends on the ability of the data to constrain the inversion for the dipole parameters. To demonstrate this process we process synthetic data collected over a 60 mm mortar. We compare results from inverting: (a) synthetically generated data for 60 mm mortars buried in a non-magnetic background and (b) data with a background geology. The synthetic data set is 70 m square, with a long wavelength background geologic response that decreases smoothly from 50 mV at the south end of the grid, and 25 mV at the north end of the grid. Correlated noise is added in the same manner as the 40 mm example presented earlier. The 60 mm mortars are buried at a depth of 50 cm.



(a) Data set with magnetic geology (left) and with the magnetic geology filtered and subtracted (right).



(b) Example of an inversion of data with a non-magnetic background

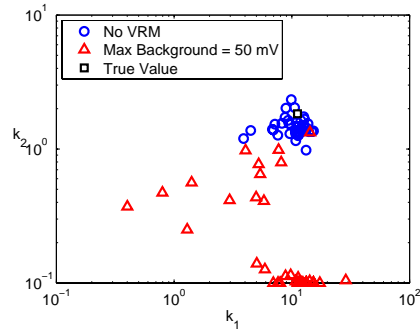


(c) Example of inversion of data with magnetic background filtered.

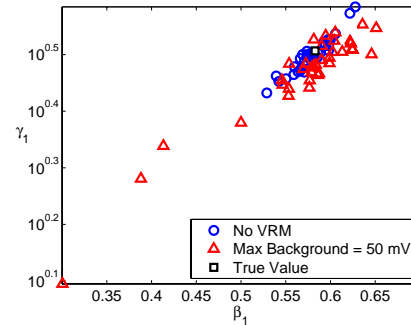
Figure 8. Inversion of synthetically generated 60 mm mortar data.

The background geology was estimated by using a low pass Butterworth filter. The background response subsequently subtracted from the observations (Figure 8(a)). Data within a 1.5 m circle radius centered about the picked targets were inverted for the dipole polarization tensor. The axial and transverse components are parameterized with the function $L(t) = kt^{-\beta} \exp(-t/\gamma)$. The dipole parameters are obtained through a least squares inversion.¹⁹ Figures 8(b) and (c) shows the data fit for a 60 mm mortar in a non-magnetic background and magnetic background, respectively. In the non-magnetic background case, the residual appears random. The magnetic background case was taken in a part of the grid where the mean background response is 50 mV. When inverting this anomaly, the residual shows background noise that appears spatially correlated.

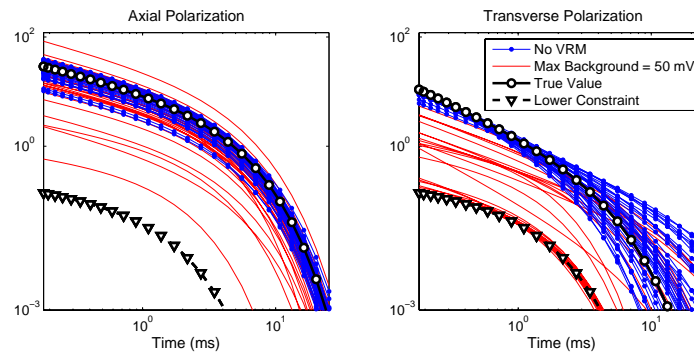
Inversion results are plotted in Figures 9. Parameters derived from the non-magnetic background data are plotted using blue circles and parameters derived from the filtered magnetic background are data plotted using red triangles. The true values are indicated by a green box. The SNR for both data sets was not high enough to constrain the estimated depth and there is a trade-off between the depth and the magnitude of the polarization amplitude. The non-magnetic background data produces a cluster near the true polarization amplitudes k_1 and k_2 values (Figure 9(a)). As Figure 8 shows, we have done a reasonably good job in removing most of the effects of the background geology. Nevertheless, the removal has not been perfect and the high frequency contaminations reduces the quality of parameters recovered from the inversion. In particular, accurate estimation of the polarization amplitudes is not possible with the filtered data. Nevertheless, some parameters appear to be more robustly recovered. The decay parameters γ_1 and β_1 are relatively well constrained (Figure 9(b)), and could be used for discrimination. Figure 9(c) shows the recovered axial and transverse polarization curves for



(a) Magnitude of the axial (k_1) and transverse (k_2) polarizations.



(b) Distribution of recovered axial polarization decay parameters γ_1 and β_1 .



(c) Recovered polarizations when inverting the 60 mm mortar data. The amplitude of the axial polarization is poorly constrained by the filtered data. Neither the amplitude nor decay behavior of the transverse polarization is well constrained by the filtered data.

Figure 9. Inversion results when fitting synthetic data over a 60 mm mortar.

the data inverted data sets. The plots confirm that the filtered magnetic background data are: (1) unable to constrain the amplitude of the axial components while correctly estimating its decay characteristics, and (2) the transverse components of the data are poorly constrained.

6. CONCLUSIONS

The most common approach to processing is to: (1) develop a target list based on a property of the data, (2) develop filtering techniques such that the background response can be estimated, and subsequently subtracted from the data, and (3) the spatially filtered data is then inverted with the physical model for the UXO response in free space. In this presentation, we looked at different aspects of processing electromagnetic data collected in regions with highly magnetic geology. Synthetic data sets were generated to help study the effectiveness of filtering, target picking, and inversion. When the soil anomalies make the target picking directly from the data difficult, the misfit to a soil model is an effective diagnostic for determining if a sounding is from soil or metal. The use of the soil model misfit was shown to be effective for picking targets in Geonics EM63 and Geophex GEM3 data acquired on Kaho'olawe. Inversion of synthetic data showed that decay characteristics of the axial polarization tensor appears to be constrained much better than the amplitude. The transverse component is not recovered well.

ACKNOWLEDGMENTS

Funding of this work is provided through the Strategic Environmental Research and Development Program (SERDP) funded project "Improving UXO Detection and Discrimination in magnetic Environments (SERDP Project MM-1414)" and U.S. Army Corps of Engineers Engineering and Research Development Center (ERDC).

REFERENCES

1. D. Cargile, H. Bennett, R. Goodson, T. DeMoss, and E. Cespedes, "Advanced uxo detection/discrimination technology demonstration - kaho'olawe, hawaii," tech. rep., U.S. Army Research and Development Center, Vicksburg, MS, 2004. ERDC/EL TR-04-1.
2. T. Lee, "The effect of a superparamagnetic layer on the transient electromagnetic response of a ground," *Geophysical Prospecting* **32**, pp. 480–496, 1983.
3. S. Billings, L. Pasion, D. Oldenburg, and J. Foley, "The influence of magnetic viscosity on electromagnetic sensors," in *Proceedings of EUDEM-SCOT2, International Conference on Requirements and Technologies for the Detection, Removal and Neutralization of Landmines and UXO*, 2003.
4. Y. Das, "Effects of soil electromagnetic properties on metal detectors," *IEEE Transactions on Geoscience and Remote Sensing* **44**(6), pp. 1444–1453, 2006.
5. S. Walker, L. Pasion, S. Billings, D. Oldenburg, and Y. Li, "Examples of the effect of magnetic soil environments on time domain electromagnetic data," in *Proceedings from SAGEEP 05*, 2005.
6. L. R. Pasion, S. D. Billings, D. W. Oldenburg, and S. E. W. and, "Application of a library based method to tem data for the identification o fuco,"
7. L. Neel, "Theorie du trainage magnetique des ferromagnetiques en grains fins avec applications aux terres cuites," *Ann. Geophys.* **5**, pp. 99–136, 1949.
8. P. C. Fannin and S. W. Charles, "On the influence of distribution functions on the after-effect function of ferrofluids," *Journal of Physics D* **28**, pp. 239–242, 1995.
9. G. R. Olhoeft and D. W. Strangway, "Magnetic relaxation and the electromagnetic response parameter," *Geophysics* **39**(3), pp. 302–311, 1974.
10. M. Dabas, J. Jolivet, and A. Tabbagh, "Magnetic susceptibility and viscosity of soils in a weak time varying field," *Geophysical Journal International* **108**, pp. 101–109, 1992.
11. G. Cross, 2006. personal communication.
12. Y. Li, R. Kahenbuhl, T. Meglich, L. Pasion, D. Oldenburg, S. Billings, D. Sinex, and S. Walker, "Improving uxo detection and discrimination in magnetic environments (serdp project mm-1414) year 1 annual report," tech. rep., Strategic Environmental Research and Development Program, 2005.
13. D. Sinex, "Advancing the state of the art of uxo discrimination for total-field magnetic data," Master's thesis, Colorado School of Mines, 2006.
14. M. S. Munkholm and E. Auken, "Electromagnetic noise contamination on transient electromagnetic soundings in culturally disturbed environments," *Journal of Engineering and Environmental Geophysics* **1**(2), pp. 119–127, 1996.
15. S. Billings, "Demonstration report for the former lowry bombing and gunnery range for estcp project 200504: Practical discrimination strategies for application to live sites," tech. rep., ESTCP, 2007.
16. I. Won, D. Keiswetter, D. R. Hanson, E. Novikova, and T. Hall, "Gem-3: A monostatic broadband electromagnetic induction sensor," *Journal of Environmental and Engineering Geophysics* **2**, pp. 53–56, March 1997.
17. T. Bell, B. Barrow, and J. Miller, "Subsurface discrimination using electromagnetic induction sensors," *IEEE Transactions Geoscience & Remote Sensing* **39**, pp. 1286–1293, 2001.
18. Y. Zhang, L. Collins, H. Yu, C. E. Baum, and L. Carin, "Sensing of unexploded ordnance with magnetometer and induction data: Theory and signal processing," *IEEE Transactions on Geoscience and Remote Sensing* **41**, pp. 1005–1015, May 2003.
19. L. R. Pasion and D. W. Oldenburg, "A discrimination algorithm for uxo using time domain electromagnetics," *Journal of Engineering and Environmental Geophysics* **6**(2), pp. 91–102, 2001.
20. S. D. Billings, "Discrimination and classification of buried unexploded ordnance using magnetometry," *IEEE Transactions Geoscience & Remote Sensing* **42**, pp. 1241 – 1251, 2004.
21. L. Collins, Y. Zhang, J. Li, H. Wang, L. Carin, S. Hart, S. Rose-Pehrsson, H. Nelson, and J. McDonald, "A comparison of the performance of statistical and fuzzy algorithms for unexploded ordnance detection," *IEEE Transactions on Fuzzy Systems* **9**, pp. 17–30, February 2001.
22. L. Beran, "Classification of unexploded ordnance," Master's thesis, University of British Columbia, 2005.